

# Low-Voltage Electrochemical $\text{Li}_x\text{WO}_3$ Synapses with Temporal Dynamics for Spiking Neural Networks

Qingzhou Wan, Marco Rasetto, Mohammad T. Sharbati, John R. Erickson, Sridhar Reddy Velagala, Matthew T. Reilly, Yiyang Li, Ryad Benosman,\* and Feng Xiong\*

Neuromorphic computing has the great potential to enable faster and more energy-efficient computing by overcoming the von Neumann bottleneck. However, most emerging nonvolatile memory (NVM)-based artificial synapses suffer from insufficient precision, nonlinear synaptic weight update, high write voltage, and high switching latency. Moreover, the spatiotemporal dynamics, an important temporal component for cognitive computing in spiking neural networks (SNNs), are hard to generate with existing complementary metal–oxide–semiconductor (CMOS) devices or emerging NVM. Herein, a three-terminal,  $\text{Li}_x\text{WO}_3$ -based electrochemical synapse (LiWES) is developed with low programming voltage (0.2 V), fast programming speed (500 ns), and high precision (1024 states) that is ideal for artificial neural networks applications. Time-dependent synaptic functions such as paired-pulse facilitation (PPF) and temporal filtering that are critical for SNNs are also demonstrated. In addition, by leveraging the spike-encoded timing information extracted from the short-term plasticity (STP) behavior in the LiWES, an SNNs model is built to benchmark the pattern classification performance of the LiWES, and the result indicates a large boost in classification performance (up to 128 $\times$ ), compared with those NO-STP synapses.


## 1. Introduction

Neuromorphic computing has emerged as a new computing paradigm to potentially overcome the von Neumann bottleneck for faster and more energy-efficient computing.<sup>[1]</sup> Despite recent advancement in computing, the human brain still outperforms computers in cognitive tasks owing to its superior energy efficiency, large parallelism, organizational hierarchy, and time-dependent neuronal and synaptic functionality.<sup>[2]</sup> Hence, researchers have been developing artificial neural networks (ANNs) to mimic the neurobiological architecture with electronics with a grand goal of building systems with general artificial intelligence (AI). Recently, deep neural networks (DNNs) have demonstrated tremendous progress for tasks, such as image classification and speech recognition.<sup>[3–10]</sup> However, these deep learning algorithms require huge amounts of computational resources, especially during the training process. Moreover, the temporal aspect in

neural spiking, an integral component for all cognitive functions in the brain (e.g., the timing difference between spikes can represent causality), has been largely omitted in DNNs—limiting

Q. Wan, M. T. Sharbati, J. R. Erickson, S. R. Velagala, M. T. Reilly, Prof. F. Xiong  
Department of Electrical and Computer Engineering  
University of Pittsburgh  
Pittsburgh, PA 15261, USA  
E-mail: f.xiong@pitt.edu

M. Rasetto  
Department of Bioengineering  
University of Pittsburgh  
Pittsburgh, PA 15260, USA

 The ORCID identification number(s) for the author(s) of this article can be found under <https://doi.org/10.1002/aisy.202100021>.

© 2021 The Authors. Advanced Intelligent Systems published by Wiley-VCH GmbH. This is an open access article under the terms of the Creative Commons Attribution License, which permits use, distribution and reproduction in any medium, provided the original work is properly cited.

DOI: 10.1002/aisy.202100021

Prof. Y. Li  
Department of Materials Science and Engineering  
University of Michigan  
Ann Arbor, MI 48109, USA

Prof. R. Benosman  
Department of Ophthalmology  
University of Pittsburgh  
Pittsburgh, PA 15213, USA  
E-mail: benosman@pitt.edu

their ability in implementing causal relationships and logical inferences. Spiking neural networks (SNNs), which aims to mimic the biological neural network more closely through incorporating the temporal components,<sup>[2]</sup> offer a promising alternative to DNNs with their excellent energy efficiencies and bandwidths from their event-driven nature, as well as their potential for cognitive computing through implementing logical inference.<sup>[11–16]</sup> However, it has been challenging and expensive to incorporate and process the spatiotemporal dynamics with existing complementary metal-oxide-semiconductor (CMOS) devices.<sup>[2]</sup>

Artificial neuronal and synaptic functionality can be mimicked by emerging nanoelectronics, such as phase change memory (PCM),<sup>[17–19]</sup> resistive random access memory (RRAM),<sup>[20–22]</sup> spin transfer torque random access memory (STT-RAM),<sup>[23,24]</sup> ferroelectric random access memory (FeRAM),<sup>[25,26]</sup> and reconfigurable photonics.<sup>[27–30]</sup> However, most of these devices are originally optimized for nonvolatile memory (NVM) applications and are, thus, unable to generate time-encoded spikes for SNNs without the use of intricate circuitries, which limits the overall cost and scalability. Recently, emerging three-terminal electrochemical redox transistors or electrochemical random access memory (ECRAM) have become a promising candidate for mimicking the biologic synapse due to its low power, high precision, linear and symmetric response, low variations, and good endurance performance.<sup>[31–39]</sup> The channel conductance (i.e., synaptic weight) of the electrochemical synapses can be continuously and controllably modulated via electrochemical reactions (e.g., involving  $\text{Li}^+$  or  $\text{H}^+$  ion flows) through a gate terminal. While  $\text{Li}^+$  ions in the gel electrolyte could potentially be a source of contamination for CMOS fabrications, it is a good material for proof-of-concept of our electrochemical redox transistors due to its well-known electrochemical behaviors. Most recently, we are able to leverage the long-term charge transfer doping effect and the short-term ionic gating effect in electrochemical transistors<sup>[39]</sup> to demonstrate tunable time-dependent spatiotemporal dynamics, which are critical for spike-based, event-driven computations.<sup>[11]</sup>

Tungsten oxide ( $\text{WO}_3$ ), consisting of corner-sharing  $[\text{WO}_6]$ -octahedral structures, can be considered as a pseudoperovskite oxide with absent A-site cations.<sup>[40,41]</sup> The absence of A-site cations can be used as interstitial space for ion intercalation and extraction,<sup>[42–44]</sup> thus making  $\text{WO}_3$  a good candidate for electrochemical synapses. Moreover, insulator-to-metal transition has been demonstrated in epitaxial  $\text{WO}_3$  film via electrolyte gating,<sup>[45–48]</sup> which provides a large conductivity modulation window for building high-precision synapses with a large dynamic range that are ideal for neuromorphic computing applications.<sup>[49]</sup> Another advantage of using  $\text{WO}_3$  film as the channel material is that the high quality epitaxial  $\text{WO}_3$  film can be deposited by radio-frequency (RF) magnetron sputtering,<sup>[48,50]</sup> providing a route toward scalable fabrications that enable the widespread of smart electronics in the era of the Internet of Things (IoTs).

While  $\text{WO}_3$ -based electrochemical synapses have demonstrated promising potentials in prior pioneering studies,<sup>[51–53]</sup> more research efforts are necessary to lower the programming voltage (e.g.,  $4\text{V}^{[53]}$ ) and improve the programming speed (e.g.,  $70\text{ms}^{[51]}$ ), two key parameters in artificial synapses. In addition, most of the prior works on  $\text{WO}_3$ -based electrochemical synapses have been focused on improving the precision for DNNs

applications with little to no effort devoted to producing time-coded spikes that are critical for SNNs applications.

In this work, we develop a three-terminal  $\text{Li}_x\text{WO}_3$ -based electrochemical synapse (LiWES) with low-programming voltage (i.e.,  $\approx 0.2\text{V}$  enabled by our self-gated design<sup>[34]</sup> with near-zero open circuit voltages (OCVs) between the gate and the channel), fast programming speed (500 ns), and high precision (1024 states) that is ideal for DNNs. We also demonstrate time-dependent synaptic functions such as paired-pulse facilitation (PPF) and temporal filtering that are critical for SNNs. In addition, by utilizing the time-encoded spikes in our LiWES dynamic synapses, we build an SNNs model to benchmark the pattern classification performance, which shows a large boost ( $128\times$  improvement) in classification performance in highly time-dependent scenarios.

## 2. Results and Discussion

### 2.1. Electrochemical $\text{Li}_x\text{WO}_3$ Synapse Structure

The structure of our LiWES is similar to that of biologic synapse, as shown in **Figure 1a**. In a biologic neural network, a synapse is the small gap (20–40 nm) between a pre-synaptic neuron and a post-synaptic neuron. This connection strength is referred to as the synaptic weight, which can be increased (potentiation) or decreased (depression) by modulating the  $\text{Ca}^{2+}$  concentration. The electrical signal from pre-synaptic neurons activates the opening of calcium channels, triggering the release of neurotransmitters from pre-synaptic neurons into post-synaptic neurons. The schematic of our three-terminal LiWES is shown in **Figure 1b**, where the channel conductance, modulated by the gate terminal, represents the synaptic weight. Tungsten oxide, which contains a large number of vacant A-sites, is ideal for reversible intercalation and de-intercalation of Li ions ( $\text{Li}^+$ ), as evident in its wide use in commercial electrochromic devices.<sup>[54]</sup> By intercalating (extracting)  $\text{Li}^+$  into (out of) the  $\text{Li}_x\text{WO}_3$  channel, we can potentiate (depress) the synaptic weight (represented by the channel conductance) of our synapse.<sup>[33,39]</sup> An optical image of the electrochemical synapse is shown in **Figure 1c**, depicting a three-terminal planar transistor structure where  $\text{WO}_3$  thin films (60 nm) are deposited on  $\text{LaAlO}_3$  (100) substrate as both the gate and the channel. Adopting the same material for both the gate and the channel allows us to minimize the OCV between the two terminals,<sup>[34]</sup> hence achieving a low programming voltage. We deposited epitaxial  $\text{WO}_3$  film on a  $\text{LaAlO}_3$  (100) substrate using RF sputtering (see the Experimental Section for fabrication processes). X-ray diffraction (XRD) (**Figure 1d**) and atomic force microscopy (AFM) (**Figure 1e**) measurements confirm the good crystallinity of the deposited  $\text{WO}_3$  film with an atomically flat surface (root-mean-square (rms) roughness  $< 600\text{pm}$ ). Having a high-quality, crystalline thin film with a smooth surface is critical for promoting the conductance modulation efficiency in our electrochemical synapse, which involves the electrolyte gating process that is sensitive to the surface smoothness.<sup>[48,50]</sup>

### 2.2. Electrochemical Modulation

In **Figure 2a**, we use  $\text{Li}_{0.6}\text{FePO}_4$  (LFP) as the  $\text{Li}^+$  ion reservoir as well as the reference gate for us to modulate the Li content in both

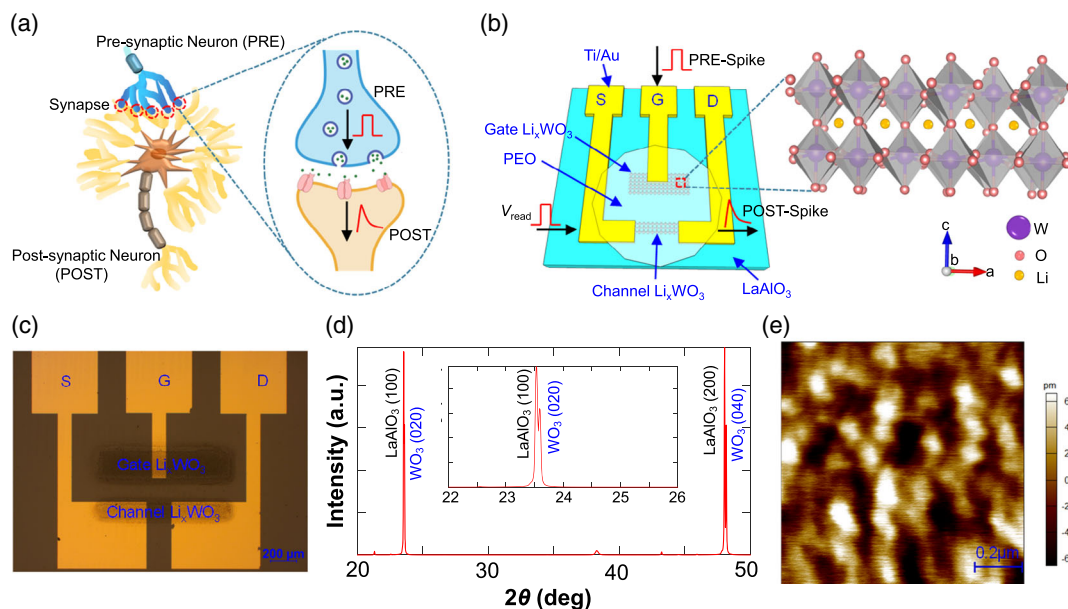


**Figure 1.** Biologic synapse compared with our LiWES and the characterization of epitaxial  $\text{WO}_3$  film. a) Biologic neuron and synapse structure. b) Schematic of our LiWES, and the inset shows the crystal structure of  $\text{WO}_3$  octahedrons. c) Optical image of the LiWES without electrolyte coating. d) XRD of the epitaxial  $\text{WO}_3$  film on  $\text{LaAlO}_3$  (100) substrate. e) AFM image of the epitaxial  $\text{WO}_3$  film, showing the atomically flat surface with an rms roughness less than 1 nm.

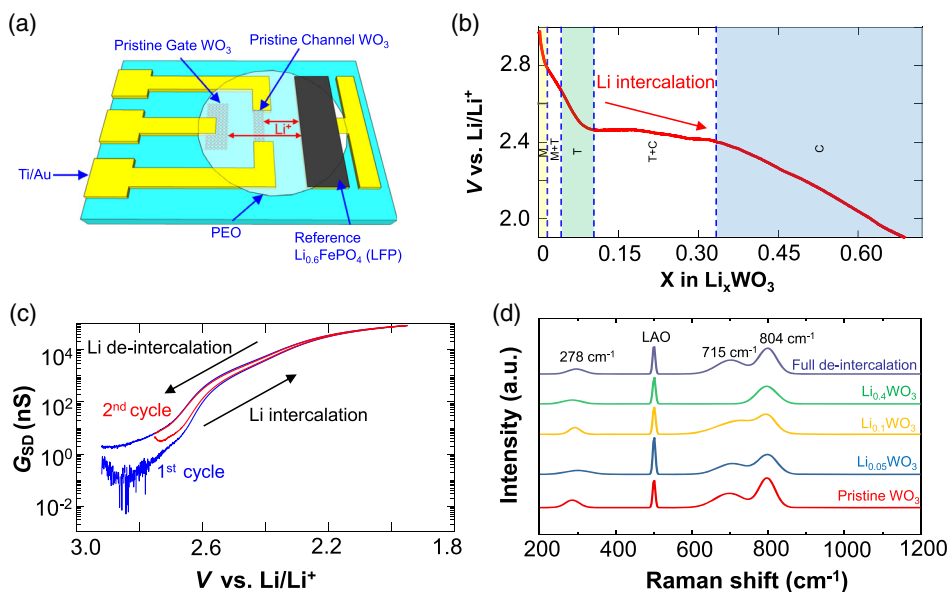


**Figure 2.** Electrochemical characterization of  $\text{WO}_3$  film during Li intercalation/de-intercalation. a) The schematic of the electrochemical cell for Li intercalation and de-intercalation. b) Galvanostatic discharge (intercalation) of  $\text{WO}_3$  film using constant current 0.1 nA during in-operando Raman spectra, indicating the electrochemical potential of  $\text{Li}_x\text{WO}_3$  change relative to the standard potential of  $\text{Li}/\text{Li}^+$  electrodes ( $V$  vs  $\text{Li}/\text{Li}^+$ ) as a function of Li concentration. c) The electrical channel conductance change as a function of the electrochemical potential of  $\text{Li}_x\text{WO}_3$  change during Li intercalation/de-intercalation. d) In-operando Raman spectra change of  $\text{WO}_3$  film during Li intercalation/de-intercalation.

the  $\text{Li}_x\text{WO}_3$  channel and self-gate, because it provides a near-constant electrochemical window ( $\approx 3.4$  V vs  $\text{Li}/\text{Li}^+$  as LFP's Li content changes from  $\text{Li}_{0.02}\text{FePO}_4$  to  $\text{Li}_{0.9}\text{FePO}_4$ ) to ensure stable operations.<sup>[55–57]</sup> We can achieve controllable tuning of the

$\text{Li}_x\text{WO}_3$  channel conductance (i.e., synaptic weight) via changing the Li content through reversible Li intercalation and de-intercalation, where Li intercalation/de-intercalation is a combination of the nonvolatile charge transfer doping and the volatile

ionic gating effects.<sup>[39]</sup> We first performed galvanostatic discharge measurements of  $\text{WO}_3$  with a constant current of 0.1 nA to establish how the electrochemical potential of  $\text{Li}_x\text{WO}_3$  relative to the standard potential of  $\text{Li}/\text{Li}^+$  electrodes ( $V$  vs  $\text{Li}/\text{Li}^+$ ) changes as a function of the Li concentration (Figure 2b). Consistent with prior studies,<sup>[42,44]</sup> the electrochemical potential of  $\text{Li}_x\text{WO}_3$  decreases, as the Li content increases. The increase of the Li content in  $\text{Li}_x\text{WO}_3$  film induces the phase transformation in a  $\text{WO}_3$  crystal structure, where the voltage plateaus correspond to the phase separation as shown in M + T and T + C labeled regions in Figure 2b. The voltage plateau in M + T region is less obvious largely likely due to the fast discharge/Li intercalation process. An advantage of our electrochemical approach over conventional resistive memory-based synapse is that it allows us to control the Li content (and, hence, the synaptic weight) in the channel accurately, enabling us to build high-precision, analog synapses<sup>[49,58]</sup> that are desirable for DNNs applications. As shown in Figure 2c, the channel conductance increases monotonically, as the Li concentration increases. This is likely because that Li ions can act as n-type dopants, increasing the channel conductance by shifting s-band high above the Fermi level with the charge-balancing electrons occupying the  $d$  conduction band in tungsten.<sup>[43]</sup> The channel conductance can be continuously modulated over four orders of magnitude, suggesting a large dynamic range that is necessary for high-precision synapse. We note that the dynamic range becomes slightly smaller after the first cycle of intercalation/deintercalation, likely due to a small amount of Li ions trapped inside the  $\text{WO}_3$  host.<sup>[54]</sup> The conductance modulation windows between the two cycles are fairly consistent, indicating a repeatable dynamic range for synaptic weight updates. Up to four consecutive cycles of the conductance modulation are shown in Figure S1a, Supporting Information, further demonstrating the good repeatability of conductance modulation in our LiWES. We also performed a control experiment with only the poly(ethylene oxide) (PEO) electrolyte (i.e., no  $\text{WO}_3$ ) (Figure S1b, Supporting Information), where we observed no change in channel conductance confirming the  $\text{Li}_x\text{WO}_3$ 's modulation. Previous studies suggest that the Li intercalation can induce phase transformation in a  $\text{WO}_3$  crystal structure,<sup>[42,44,46,47]</sup> where the  $\text{Li}_x\text{WO}_3$  film goes through phase transformations from monoclinic ( $0 < x < 0.01$ ), tetragonal ( $0.05 < x < 0.12$ ), to cubic ( $0.32 < x < 0.7$ ) with increased crystal symmetry, as its Li content increases, partly accounting for the electrical properties change in  $\text{Li}_x\text{WO}_3$  films.<sup>[42,43,46]</sup> As shown in Figure 2b,c, nonlinearity behavior exists due to the phase transformation of  $\text{WO}_3$  crystal, which is why it is important to lithiate the  $\text{WO}_3$  channel and modulate its electrical conductance during the cubic phase region for obtaining a more linear response. Our in-operando Raman measurements (see the Experimental Section for Raman setup) in Figure 2d suggests similar crystal structure changes during the lithiation process. Two strongest peaks in Raman spectra of  $\text{WO}_3$  film are located at  $\approx 715$  and  $\approx 804$   $\text{cm}^{-1}$ , corresponding to the asymmetric and symmetric stretching vibrations of  $\text{W}^{6+}-\text{O}$  bonds, whereas the peak at  $\approx 278$   $\text{cm}^{-1}$  is due to the bridging  $\text{O}-\text{W}-\text{O}$  bonds.<sup>[59,60]</sup> The intercalation of Li ions induces a larger lattice distortion, forcing the crystal structure to become more symmetric, which leads to the gradual diminishing of the peak at  $715$   $\text{cm}^{-1}$  as well as a blue shift of the peak from  $\approx 804$  to  $\approx 806$   $\text{cm}^{-1}$ , resulting from the slightly decreased lattice parameters of  $\text{Li}_x\text{WO}_3$  bronzes.<sup>[44]</sup>

### 2.3. Low-Voltage and High-Precision Synapses

While LFP serves as a good reservoir of Li ions due to its stable electrochemical window, it is not an ideal control gate for a three-terminal artificial synapse, because it would require a high programming voltage to overcome the electrochemical potential difference (ranging from  $\approx 0.45$  to  $1.45$  V)<sup>[44]</sup> between the channel ( $\text{Li}_x\text{WO}_3$ ) and the gate (LFP). Hence, we adopt a self-gate structure, where we use the same material ( $\text{Li}_x\text{WO}_3$ ) for both the channel and the control gate, hence minimizing the potential difference<sup>[34]</sup> as well as achieving sub-1 V operations. We first lithiated both as-deposited  $\text{WO}_3$  gate and  $\text{WO}_3$  channel to the same lithiation levels ( $\text{Li}_{0.4}\text{WO}_3$ ) through applying a constant voltage bias  $V_{\text{Li}_x\text{WO}_3} = -1.1$  V on both the gate and the channel while grounding the LFP reference,<sup>[34]</sup> allowing us to achieve a near-zero OCV ( $< 0.1$  V) between the gate and the channel as well as a cubic  $\text{WO}_3$  crystal structure for obtaining a more linear conductance response via pulse modulation. We envision that only one global LFP gate is needed as the ionic reservoir for a self-gated synaptic array, where pre-charge operations (to charge the self-gate to the desired electrochemical level) are sparingly performed. This will enable low-voltage programming as well as both short-term plasticity (STP) and long-term plasticity (LTP) while keeping the fabrication and circuitry design complexity at a manageable level.

Combining this with the high-precision nature of our synapse originating from the large dynamic range as well as the good tunability enabled by the electrochemical intercalation, we demonstrate both potentiation and depression functions in Figure 3a with low programming voltages (0.5 V) and good precision (1024 distinct states). We applied 512/1024 potentiation pulses (0.5 V, 10 ms) and 512/1024 depression pulses ( $-0.5$  V, 10 ms) at  $\text{Li}_{0.4}\text{WO}_3$  self-gate, where we observed a relatively linear and symmetric weight updates. We note a tradeoff between the dynamic range and linearity/symmetry, where the linearity and symmetry of conductance response are slightly reduced when a larger number of pulses are used to push the synapse to a larger dynamic range, likely associated with the saturation of accumulated electric charges at the interface between the  $\text{Li}_x\text{WO}_3$  channel/electrolyte and the asymmetry of electric charges accumulation (potentiation) and release (depression) processes under different directions of electric fields. In biological synapses, the amount of weight change (represented by the change in channel conductance  $\Delta G_{\text{SD}}$  in our device) often varies for different neuronal signals.<sup>[61]</sup> We can mimic this behavior in our synapse to achieve different  $\Delta G_{\text{SD}}$  values by varying the amplitude, width, and numbers of the programming pulse(s), as shown in Figure 3b–d. We observed pseudo-linear relationships between  $\Delta G_{\text{SD}}$  with respect to the pulse amplitude (from 0.1 to 2 V, Figure 3b) and width (from 10 to 500 ms, Figure 3c), respectively. This is likely because  $\Delta G_{\text{SD}}$  is dependent on the amount of Li ions being transferred into the  $\text{Li}_x\text{WO}_3$  film during the programming pulse. We observe a similar pseudo-linear relationship between  $\Delta G_{\text{SD}}$  and the pulse number up to 800 pulses, after which  $\Delta G_{\text{SD}}$  starts to become saturated. This saturation behavior is likely due to the limited amount of Li ions that can be transferred into the channel at a given electrochemical potential between the channel and the gate, which is dictated

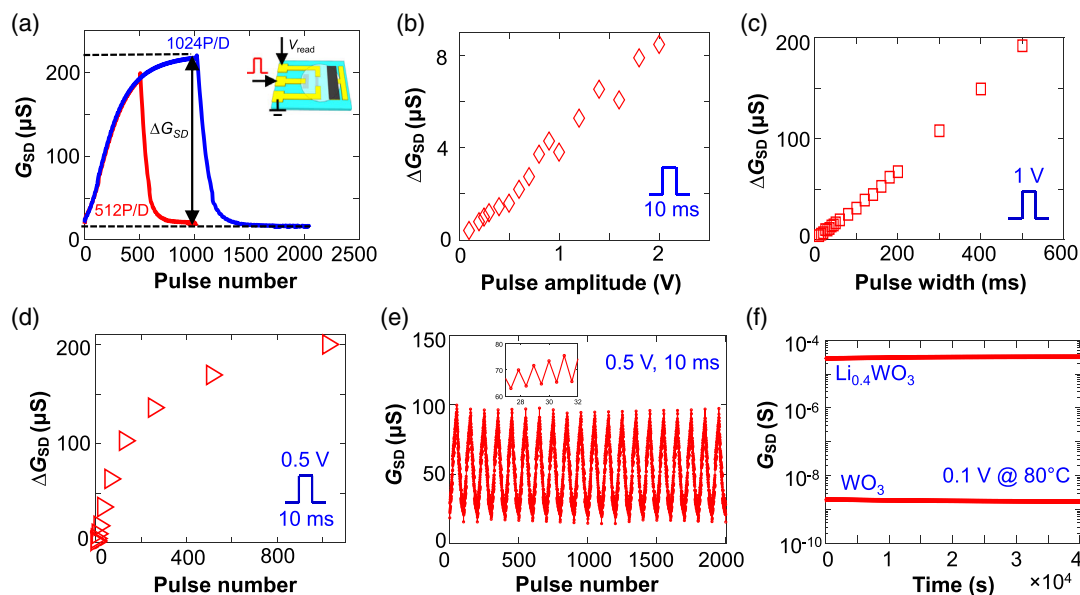


**Figure 3.** Synaptic weight modulation for DNNs application using our low-voltage LiWES. a) Dynamic range and precision controlled using different numbers of programming potentiation pulses (0.5 V, 10 ms) and depression pulses (−0.5 V, 10 ms) at  $\text{Li}_{0.4}\text{WO}_3$  gate (the inset). b) Synaptic weight change as a function of pulse amplitude. c) Synaptic weight change as a function of pulse width. d) Synaptic weight change as a function of pulse number. e) Endurance test using 20 cycles of 50 potentiation pulses (0.5 V, 10 ms) and 50 depression pulses (−0.5 V, 10 ms) at  $\text{Li}_{0.4}\text{WO}_3$  gate. f) Stability test for two different states: pristine  $\text{WO}_3$  and  $\text{Li}_{0.4}\text{WO}_3$  (initial conductance state for self-gate and channel), using a reading voltage of 0.1 V at 80 °C.

by the pulse amplitude (i.e., 0.5 V in Figure 3d) and the lithiation concentration in the channel.

To study the endurance behavior of our synapse, we cycled our synapse over 2000 pulses (20 cycles of 50 potentiation (0.5 V, 10 ms) and 50 depression (−0.5 V, 10 ms) pulses, as shown in Figure 3e), where we observed reversible and repeatable conductance change with a 500% dynamic range. We also performed long-time endurance test for  $10^5$  pulses on LiWES (Figure S2, Supporting Information), where the synapse showed no sign of degradation after  $10^5$  pulses. We carried out thermal stability test for two different states: pristine  $\text{WO}_3$  (before lithiation) and  $\text{Li}_{0.4}\text{WO}_3$  (initial conductance state for self-gate and channel after lithiation), where we observed minimal resistance drift over 11 h at 80 °C for both states (Figure 3f). By statistically analyzing the conductance change  $\Delta G_{\text{SD}}$  per pulse in Figure 3e, we observe small temporal (pulse-to-pulse) variations for potentiation pulses and depression pulses, as shown in Figure S3a, Supporting Information. In addition, we studied  $\Delta G_{\text{SD}}$  per pulse for four different devices and observed a small device-to-device variation of  $\approx 6.5\%$  (Figure S3b, Supporting Information), suggesting good repeatability and scalability of our devices.

#### 2.4. Temporal Dynamics

For SNNs, a dynamic synapse with both LTP and STP is essential for learning applications. However, it has been difficult to implement such temporal dynamics with traditional CMOS devices. Our LiWES naturally possesses both LTP and STP, owing to a combination of the volatile ionic gating (Figure 4a) and the non-volatile charge transfer doping (Figure 4b) effects. Nonvolatile charge transfer doping effect results in LTP, as intercalated Li

ions could stay at vacant A-sites in pseudo-perovskite tungsten oxide for a long time via the electrochemical reaction (Figure 4b) as  $\text{Li}_{0.4}\text{WO}_3 + x\text{Li}^+ + xe^- \leftrightarrow \text{Li}_{0.4+x}\text{WO}_3$ , whereas volatile ionic gating effect results in electrical double layer formation (Figure 4a). The ionic gating effect is short term, because the accumulated electric charges ( $\text{Li}^+$  ions in the PEO electrolyte) at the interface between  $\text{Li}_x\text{WO}_3$  channel and electrolyte would quickly diffuse back to the electrolyte when the external applied electric field (gate voltage) is removed. We are able to achieve the transition of STP to LTP by switching from a  $\text{Li}_x\text{WO}_3$  self-gate to an LFP reference gate. As shown in Figure 4c, the  $\text{Li}_x\text{WO}_3$  self-gate is used to apply voltage pulses, which enables a low programming voltage ( $\approx 0.2$  V) owing to the near-zero OCV between  $\text{Li}_x\text{WO}_3$  self-gate and channel. We observed a spike in channel conductance after the programming pulse due to ionic gating effects. As the volatile ionic gating effect dissipates after the voltage pulse, the channel conductance returns toward its original value. In this case, we observed no obvious charge transfer doping effect (LTP), likely because the electrochemical reaction driving force (electrochemical potential differences between gate and channel) for LTP is weak, because there is a near-zero OCV between  $\text{Li}_x\text{WO}_3$  self-gate and channel. By switching from the self-gate to an LFP gate (Figure 4d), we observed a spike in channel conductance likely due to combined ionic gating [ $\Delta G_{\text{ST}}(t)$ ] and charge transfer doping effects [ $\Delta G_{\text{LT}}(t)$ ]. As the electrochemical OCV between LFP gate and  $\text{Li}_x\text{WO}_3$  channel is  $\approx 1.1$  V, there is enough electrochemical reaction driving force for charge transfer doping effect, and thus, the resulting time-dependent channel conductance consists of a long-term component [ $\Delta G_{\text{LT}}(t)$ ] and a time-dependent, short-term component [ $\Delta G_{\text{ST}}(t)$ ], such that  $\Delta G_{\text{SD}}(t) = \Delta G_{\text{LT}} + \Delta G_{\text{ST}}(t)$ . We achieved long-term potentiation

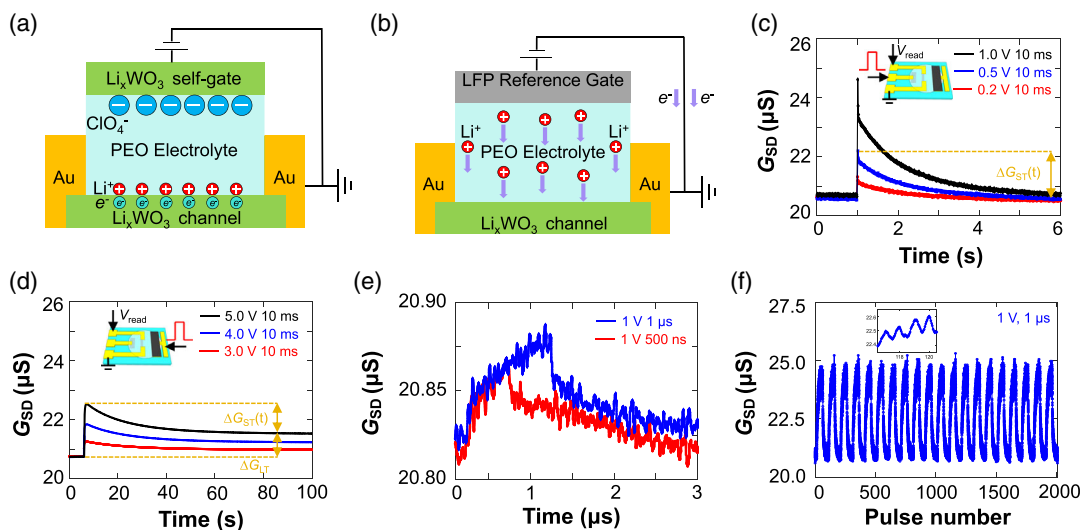


**Figure 4.** STP, LTP, and high-speed programming of our LiWES. a) Ionic gating effect for STP. b) Charge transfer doping effect for LTP, where the electrochemical reaction occurs as  $\text{Li}_{0.4}\text{WO}_3 + x\text{Li}^+ + xe^- \leftrightarrow \text{Li}_{0.4+x}\text{WO}_3$ , which is a type of donor doping. c) STP using  $\text{Li}_{0.4}\text{WO}_3$  gate and  $\text{Li}_{0.4}\text{WO}_3$  channel, controlled by different amplitudes of single pulse at  $\text{Li}_{0.4}\text{WO}_3$  gate side. The inset shows the test setup. d) LTP using LFP gate and  $\text{Li}_{0.4}\text{WO}_3$  channel, controlled by different amplitudes of single pulse at LFP gate. The inset shows the test setup. e) High-speed programming using different widths of single pulse applied at  $\text{Li}_{0.4}\text{WO}_3$  self-gate. f) Synaptic weight modulation via 20 cycles of 50 potentiation pulses (1 V, 1  $\mu\text{s}$ ) and 50 depression pulses (−1 V, 1  $\mu\text{s}$ ) applied at  $\text{Li}_{0.4}\text{WO}_3$  self-gate.

and depression via applying multiple pulses at LFP gate, as shown in Figure S4a, Supporting Information. We also studied the long-time stability for the intermediate conductance states during long-term potentiation and depression (Figure S4b,c, Supporting Information), where minimal stability degradation was observed. We also investigate how the pulse duration may affect the amount of weight change using  $\text{Li}_x\text{WO}_3$  self-gate (Figure 4e). We still observe STP due to ionic gating with pulses as short as 500 ns, consistent with the time scale reported in the literature for ionic gating and electrical double layer formation.<sup>[62]</sup> The amount of STP decreases, as the pulse duration decreases, likely because smaller amount of electric charges accumulate at the interface between  $\text{Li}_x\text{WO}_3$  channel/electrolyte and, thus, induce less electrons inside the  $\text{Li}_x\text{WO}_3$  channel in shorter pulses. In addition, we are able to achieve consistent weight updates over 20 cycles of 50 potentiation (1 V, 1  $\mu\text{s}$ ) and 50 depression (−1 V, 1  $\mu\text{s}$ ) pulses, with similar linearity and symmetry (Figure 4f) compared with long pulses (10 ms, Figure 3e).

In addition to LTP and STP, time-encoded spikes containing rich temporal information, which are responsible for learning and logical inference in biological neural network, are also desirable for SNNs applications. To better focus on studying temporal dynamics of our synapses, the benchmark of their performance in DNNs would be omitted here, but we believe our LiWES synapses could potentially demonstrate decent DNNs performance because of their small energy consumption ( $\approx 2$  pJ) for a single pulse event (Figure S5, Supporting Information), fast programming speed, high precision, and low variations. Leveraging the natural decay in our synapses, we demonstrate time-dependent synaptic functions such as PPF and temporal filtering in Figure 5, which have been difficult to implement with traditional CMOS devices. Tunable conductance change  $\Delta G$  for a pair of

pulses can be achieved by adjusting the time interval ( $\Delta t$ ) between these two pulses at  $\text{Li}_{0.4}\text{WO}_3$  self-gate (Figure 5a), mimicking the short-term, dynamic phenomenon in biological neural network where the amplitude of the second response is dependent on how closely the two pulses are related.<sup>[63]</sup> In particular, the incremental effect ( $G_2 - G_1$ ) in our synapse becomes less, as the time interval becomes longer, as shown in Figure 5b. This resembles the biological learning behavior where the learning effect is better reinforced when two stimulations are more closely related. We also fit two characteristic timescales with a two-term exponential function:  $\tau_1 = 19$  ms and  $\tau_2 = 433$  ms, which are consistent with those found in biological synapse<sup>[63]</sup> and other previously reported artificial synapses.<sup>[32,33]</sup> Those two characteristic timescales are likely related to the diffusion dynamics of Li ions<sup>[32,33,39,51]</sup> and can be engineered by changing the device dimension as demonstrated in prior studies.<sup>[32,39]</sup> We also examine how the programming energy scales as we vary the dimensions and observe promising scalability down to a channel area of  $50 \times 200 \mu\text{m}^2$  (Figure S5, Supporting Information). STP can be used to generate filtering functions that are used in information processing, e.g., fish view, the surrounding environment through the low-pass temporal filtering by which activated patterns of slow frequency ( $< 10$  Hz) are passed while repetitive patterns of fast frequency ( $> 10$  Hz) are rejected.<sup>[64]</sup> The frequency-dependent high-pass temporal filtering can be mimicked by short-term facilitation (STF).<sup>[65,66]</sup> By varying the signal frequency (i.e., time interval between pulses), we can modulate the maximum conductance level of our device, mimicking a high-pass temporal filtering. As we increase the frequency of a pulse train consisting of ten consecutive pulses (0.5 V, 10 ms for each pulse) from 1 to 80 Hz at  $\text{Li}_{0.4}\text{WO}_3$  self-gate (Figure 5c), the maximum obtainable conductance level

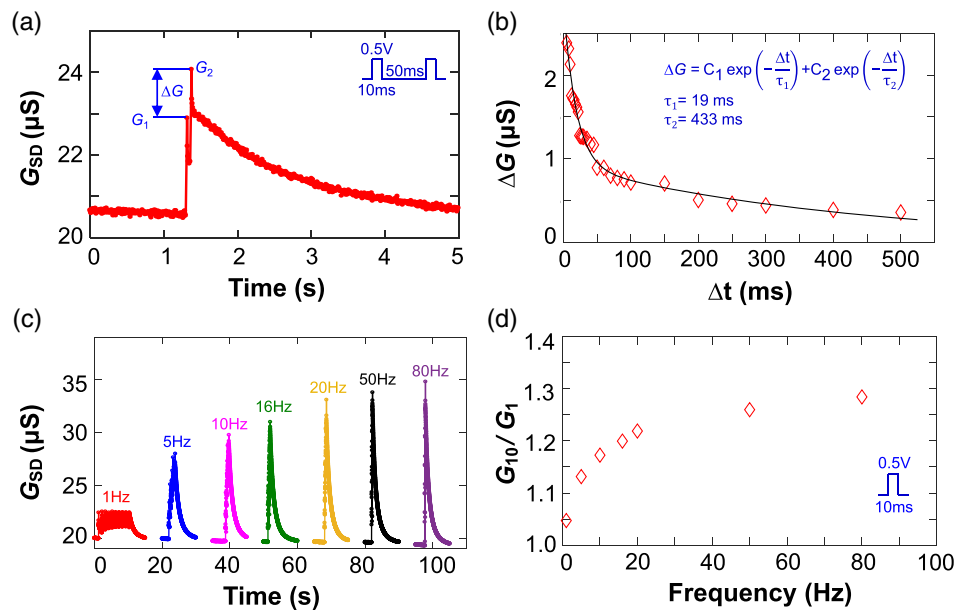


**Figure 5.** Bio-realistic, time-dependent synaptic functions for SNNs. a) Two consecutive pulses (0.5 V, 10 ms,  $\Delta t = 50$  ms) at  $\text{Li}_{0.4}\text{WO}_3$  gate showing PPF. b) PPF with exponential decay fitting. c) High-pass temporal filtering characteristics of our LiWES via applying ten potentiation pulses (0.5 V, 10 ms) with different frequencies ( $1/\Delta t$ ) at  $\text{Li}_{0.4}\text{WO}_3$  gate. d) The frequency-dependent conductance gain.

increases.<sup>[65]</sup> We also studied frequency-dependent gains of high-pass temporal filtering (Figure 5d), where the gain is defined as the ratio of the maximum conductance level of the tenth pulse ( $G_{10}$ ) to the first pulse ( $G_1$ ), demonstrating our LiWES can act as a high-pass temporal filter for information processing that is highly desirable for temporal computation in SNNs.

## 2.5. SNNs Computation Implementing Temporal Spiking Information

The goal of this section is to show how our LiWES devices' dynamic behaviors could be used to boost classification performance in highly time-dependent scenarios. The principle behind the proposed computation is that when the LiWES devices receive a set of spikes, their conductance value will change depending on the temporal structure (individual spike timings) of the input spike train (Figure 5). Furthermore, in the absence of LTP when using  $\text{Li}_x\text{WO}_3$  self-gate and channel, the conductance of the device will be uniquely determined by the input spiking pattern and the time of integration,<sup>[11,67]</sup> granting the device the ability to integrate temporal information and distinguish between different spike patterns.

In standard neuromorphic SNNs with NO-STP synapses, the synaptic efficacy (or weight), which remains fixed during inference, is used to simply scale current pulses directed toward the post-synaptic neuron. In these models, the temporal integration of stimuli is left solely to the neuron; whereas in STP-enabled networks, synapses also encode temporal information through weight changes, enriching network dynamics<sup>[65,68,69]</sup> and increasing the ability of neurons to discriminate between temporal stimuli.<sup>[70]</sup> For this reason, when compared with NO-STP synapses, a network including the proposed LiWES device should

increase its performance in highly time-dependent tasks, such as classification of different spike patterns. To test this hypothesis, we propose a test tailored to compare our LiWES to an IDEAL synapse (a noiseless LiWES device) and a standard NO-STP synapse. Here, we connect a post-synaptic neuron, modeled with Leaky Integrate and Fire profile (parametrized with the membrane decay constant  $\tau_m$  and spiking threshold  $= \infty$ ), to a pre-synaptic neuron, which is a Poisson Spike generator (Figure 6a). As shown in Figure 4c, the channel conductance response of our LiWES shows a spike profile, where the conductance quickly reaches the maximum conductance level followed by an exponential decay back to initial conductance level, due to ionic-gating governed STP effect. Thus, we are able to model the conductance response of our LiWES with a linear rise equation (gate-pulse applied) and a double exponential decay equation (gate-pulse removed). (See the Experimental Section for model build details.) Every time the synapse receives a new spike at the time  $t_i$ , the parameter  $G_{\text{off}}$  gets updated to the last conductance value, whereas a set of parameters are drawn to generate a response as the one shown in Figure 6b.

In the proposed task, we generate multiple pre-synaptic neuron spike trains with a fixed maximum duration. As each spike sequence is randomly generated at a fixed frequency, therefore, it differs from the others mainly by its temporal characteristics (the timestamps of individual spikes), and it represents a single class of a classification problem. The beginning of each spike train is delimited by  $t_{\text{onset}}$ . A "sequence end spike" is added at the end of each spike train at a specific time  $t_{\text{end}}$  (Figure 6c), and the post-synaptic neuron membrane potential is read out at  $t_{\text{read}}$  (Figure 6d), representing the output of the system. Each spike train is presented to the synapse multiple times to obtain multiple membrane potential readouts for the same "class" (or spike

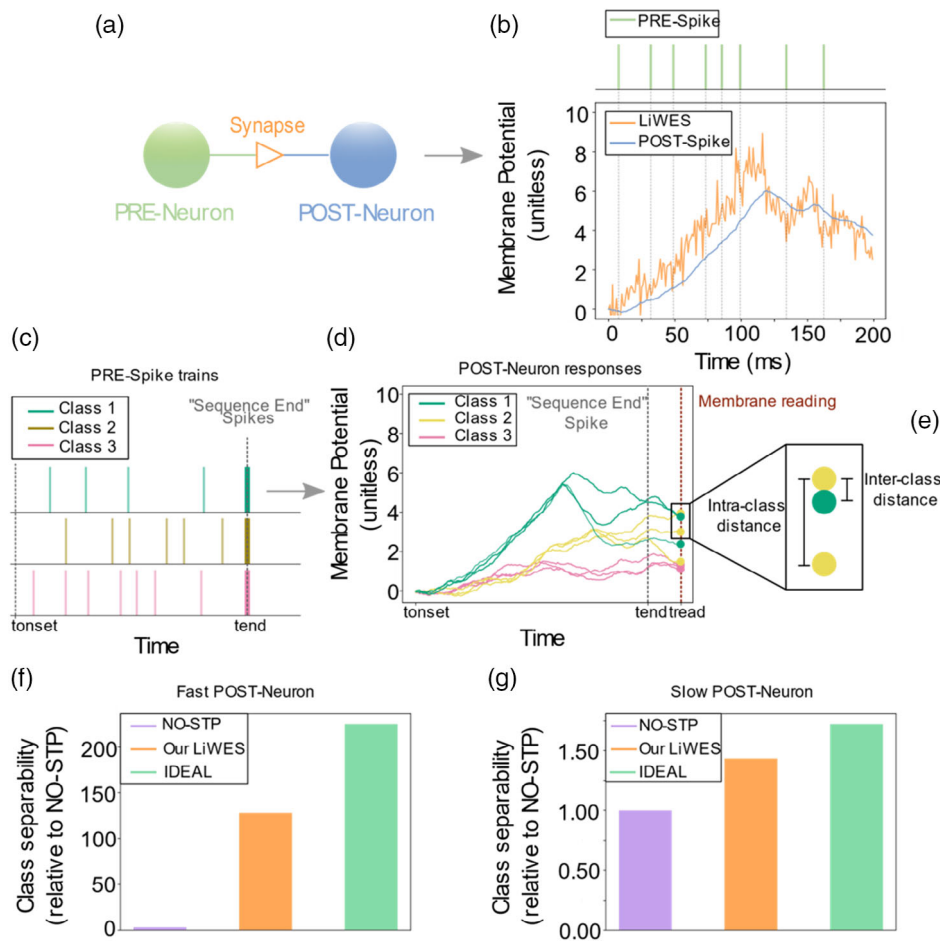


**Figure 6.** SNNs computation-based STP of our LiWES. a) The diagram of our network, a Poisson pre-synaptic (PRE) neuron connected to a Leaky and Integrate and Fire post-synaptic (POST) neuron through a synapse (NO-STP, our LiWES or IDEAL synapse). b) An example of a Poisson train spike eliciting activity in our LiWES and the consequently generated membrane potential. c–e) An example of the proposed spike-based SNNs computation model for classification performance benchmark. c) The PRE-Neuron produces multiple random spike trains; at the end of each one, we add a “sequence end” spike occurring always at the same timestamp ( $t_{\text{end}}$ ). Each spike train represents a different class in a classification problem. d) We then record multiple POST-Neuron responses (three responses per each spike train), to better characterize the device noise and cycle-to-cycle variation, and finally, we save the membrane value after the “sequence end spike” (at  $t_{\text{read}}$ ). e) Finally, for each point, we calculate the interclass distance between points of different spike trains and the intraclass distance between points of the same spike train class. These measures indicate how much each point position encodes for temporal information, and how well the points are separable in a classification task. f, g) The classification result of the benchmarked synapses. f) The classification comparison for a 10 Hz Poisson PRE-Neuron and a fast POST-Neuron ( $\tau_m = 10$  ms). g) The classification comparison for the same 10 Hz Poisson PRE-Neuron but a much slower POST-Neuron ( $\tau_m = 100$  ms).

pattern). To calculate the class separability of the readouts, we define a distance metric as the difference between the Euclidean distance of points between different classes (interclass distance) and the distance of the points within the same class (intraclass distance) in Figure 6e. As the membrane potential of the post-synaptic neuron is always read out at the same time ( $t_{\text{read}}$ ) after the last spike ( $t_{\text{end}}$ ), a neuron unable to integrate temporal information will have similar membrane potential for different spike patterns, and therefore, it will have an average interclass distance of zero or close to zero. However, for an STP-enabled neuron, its membrane value depends on previous spiking activity, which gives different values of interclass distance based on different classes. This is the case shown in Figure 6f, where a fast spiking neuron ( $\tau_m = 10$  ms) is stimulated

with Poisson generated spikes at a slow mean of 10 Hz frequency. The number of classes used for this simulation was 50, each one presented ten times (for intraclass measurement), for a total number of 500 points. In this case, class separability (interclass distance–intraclass distance) is  $\approx 3.8 \times 10^{-4}$  for the NO-STP synapse,  $\approx 4.9 \times 10^{-2}$  for our LiWES device ( $\approx 128 \times$  higher relative to NO-STP synapse), and  $\approx 8.6 \times 10^{-2}$  for the IDEAL synapse ( $\approx 226 \times$  higher compared with NO-STP synapse), with using a synaptic weight  $k$  of 4.3 (see the Experimental Section for model build details). As both comparison synapses (NO-STP and IDEAL synapses) are totally deterministic, their mean intraclass distance is 0. The same simulation parameters are used in Figure 6g for a much slower post-synaptic neuron ( $\tau_m = 100$  ms). Even though the post-synaptic neuron is relatively



**Table 1.** Model parameters for a single pulse (1 V, 200  $\mu$ s). Results of an averaged fit over 20 consecutive recordings. All parameters are presented with their mean  $\pm$  standard deviation except for  $\eta$ , which is the mean standard deviation of each individual fit.

$A_1$	$\tau_1$ [ms]	$A_2$	$\tau_2$ [ms]	$\eta$
$0.57 \pm 0.27$	$5 \pm 2$	$0.5 \pm 0.05$	$92 \pm 18$	0.11

slower to integrate temporal information, a boost in class separation ( $\approx 1.4\times$  in our LiWES and  $\approx 1.7\times$  in the IDEAL synapse, relative to the NO-STP synapse) can still be achieved owing to the natural stochastic STP in our LiWES. The class separability is  $\approx 8.4 \times 10^{-2}$ ,  $\approx 1.2 \times 10^{-1}$ , and  $\approx 1.4 \times 10^{-1}$ , for the NO-STP synapse, our LiWES device, and the IDEAL synapse, respectively, with using a synaptic weight  $k$  of 16.7. By implementing the temporal spiking information in STP of our LiWES, we improve the pattern classification performance (up to  $128\times$  compared with NO-STP synapse) in highly time-dependent scenarios.

### 3. Conclusion

In summary, we develop a  $\text{WO}_3$ -based, electrochemical synapse with low programming voltage (0.2 V), fast programming speed (500 ns), high precision (1024 levels), low variations, and a relatively linear and symmetric response. In addition, our dynamic synapse naturally exhibits both LTP and STP behaviors owing to the combined effects from charge transfer doping and ionic gating, which is desirable for SNNs applications. We demonstrate various time-dependent synaptic functions such as PPF and temporal filtering. By leveraging the spike-encoded timing information extracted from the STP exponential decay behavior, we build an SNNs model to benchmark the pattern classification performance of our LiWES, which shows a large boost ( $128\times$  improvement) in classification performance in highly time-dependent scenarios.

### 4. Experimental Section

**Fabrication of Electrochemical  $\text{WO}_3$  Synapses:** Epitaxial tungsten oxide ( $\text{WO}_3$ ) thin films were deposited on (100)  $\text{LaAlO}_3$  substrates (MTI Ltd.) using RF magnetron sputtering with  $\text{WO}_3$  target (99.99% purity from Sigma-Aldrich). A total RF power of 80 W was used. The process pressure was kept at 60 mTorr with a gas ratio of 1:2 for  $\text{Ar}:\text{O}_2$ , whereas the deposition temperature was kept at 650  $^\circ\text{C}$  to achieve a deposition rate at 1 nm  $\text{min}^{-1}$ . The resulting  $\text{WO}_3$  film thickness was 60 nm, measured by a surface profiler (KLA-Tencor AlfaStep IQ). During the deposition of  $\text{WO}_3$  film, a shadow mask was used for patterning. Devices of different channel areas (from  $1000 \times 200$  to  $200 \times 50 \mu\text{m}^2$ ) were fabricated for variation study. For the electrical characterization and pulse measurement, the devices of  $400 \times 200 \mu\text{m}^2$  channel area were used. Au contacts (100 nm) with a Ti adhesion layer (5 nm) were deposited using an electron-beam evaporator and patterned by a shadow mask. The deposited Ti/Au metal contacts are on top of the as-grown  $\text{WO}_3$  film.

The reference gate LFP was placed about 2 mm away from the  $\text{WO}_3$  channel. The LFP gate was prepared by manually coating the LFP slurry<sup>[34]</sup> onto a Au contact pad. The PEO electrolyte was prepared by mixing 30 wt%  $\text{LiClO}_4$  (Sigma-Aldrich) with PEO (molecular weight 600 000 from Sigma-Aldrich) in acetonitrile solvent. Subsequently, the PEO electrolyte ( $\approx 1 \mu\text{m}$ )<sup>[71]</sup> was drop-casted to cover both the  $\text{WO}_3$  gate/channel and

the LFP reference gate. The PEO serves as an electrolyte for  $\text{Li}^+$  ions transport in both the cases:  $\text{Li}_x\text{WO}_3$  self-gate and channel, and LFP gate and  $\text{Li}_x\text{WO}_3$  channel. The difference between self-gate and LFP gate is the OCV between gate and channel as well as the required programming voltage. To remove the residual solvent, the sample was heated at 80  $^\circ\text{C}$  on a hot plate overnight. All the chemical preparation and operation steps were performed in an Ar gas glovebox.

**XRD and AFM Characterization:** The Bruker D8 Discover instrument was used for XRD measurement. The  $\text{WO}_3$  film sample for XRD was annealed at 650  $^\circ\text{C}$  in air for 1 h. The asylum MFP-3D was used for AFM measurement, and a scan area of  $1 \times 1 \mu\text{m}^2$  was chosen for surface roughness analysis.

**Raman Spectroscopy:** The Horiba Scientific system with a 633 nm laser (1800  $\text{g mm}^{-1}$  grating) was used for in-operando Raman measurements. The absorbed laser power was kept low ( $<5$  mW) to avoid excessive laser heating.

**Electrochemical Characterization:** Electrochemical galvanostatic discharge measurement was carried out with an SP-200 Biologic workstation. A constant discharge/charge current of 0.1 nA was applied with the  $\text{WO}_3$  channel connected to the working electrode and the LFP reference gate connected to the counter/reference electrodes. To convert the electrochemical potential of  $\text{Li}_x\text{WO}_3$  (vs. LFP) to the potential (vs.  $\text{Li}/\text{Li}^+$ ), a value of 3.4 V is added to the measured electrochemical potential of  $\text{Li}_x\text{WO}_3$  (vs. LFP).

**Electrical Characterization and Pulse Measurement:** Electrical characterization and pulse measurement were performed with Keithley Semiconductor Parameter Analyzer (4200-SCS) with pulse measuring units. During the test, the sample was transferred into the vacuum probe station (JANIS ST-500-UHT) and annealed at 350 K for  $\approx 2$  h to eliminate the residual moisture before the electrical measurements. For fast-speed pulse tests, an arbitrary function generator (Tektronix AFG3252C) and a mixed domain oscilloscope (Tektronix MDO 3034) with a high-speed current amplifier (FEMTO DHPA-100) were used via a customized LABVIEW program.

**SNN Computation Model:** We model our LiWES device behavior using a linear rise (Equation (1)) and a double decay exponential model (Equation (2)), using Equation (3) to define the rise and decay parts, respectively.

$$G_{\text{rise}}(t) = (\widehat{A}_1 + \widehat{A}_2) \frac{t - t_i}{w} + \eta + G_{\text{off}} \quad (1)$$

$$G_{\text{decay}}(t) = \left( \widehat{A}_1 + \frac{G_{\text{off}}}{2} \right) e^{-\left(\frac{t-t_i}{\tau_1}\right)} + \left( \widehat{A}_2 + \frac{G_{\text{off}}}{2} \right) e^{-\left(\frac{t-t_i}{\tau_2}\right)} + \eta \quad (2)$$

$$G(t) = \begin{cases} G_{\text{rise}}(t) & \text{when } (t - t_i) < w \\ G_{\text{decay}}(t) & \text{when } (t - t_i) \geq w \end{cases} \quad (3)$$

The model parameters ( $\widehat{A}_1, \widehat{A}_2, \widehat{\tau}_1, \widehat{\tau}_2$ ) are drawn from Gaussian distributions fitted on experimental recordings obtained with a single pulse stimulus of a given amplitude and pulse width  $w$ . Additive Gaussian noise  $\eta$  with a mean of 0 is also added to simulate device and recording setup noise.

To obtain the Gaussian distributions of the LiWES parameters ( $\widehat{A}_1, \widehat{A}_2, \widehat{\tau}_1, \widehat{\tau}_2$ ) and the standard deviation of the additive noise, we fit the decay equation (Equation (2)) on the device response to a single pulse (1 V, 200  $\mu$ s) for 20 consecutive trials. Every trial produces a set of parameters ( $A_1, A_2, \tau_1, \tau_2, \eta$ ), which can then be averaged to produce **Table 1**.

When simulating the noise-free, IDEAL synapse, we use the same parameters mentioned earlier, but set all standard deviations and additive Gaussian noise  $\eta$  to 0. Finally, the NO-STP synapse is modeled as a weighted Dirac pulse centered on the input spike timestamp  $t_i$  (Equation (4)).

$$G(t) = \sum_{t_i} k\delta(t - t_i) \quad (4)$$

where  $k$  is the synaptic weight chosen, so that the peak response of the post-synaptic neuron to a single spike is the same to the IDEAL synapse.

## Supporting Information

Supporting Information is available from the Wiley Online Library or from the author.

## Acknowledgements

M.R. and M.T.S. contributed equally to this work. Q.W., M.T.S., J.R.E., S.R.V., M.T.R., and F.X. acknowledge support from the National Science Foundation (NSF) 1909797, 1943683, 1901864, and 1955453. This work was performed, in part, at the Nanoscale Fabrication and Characterization Facility, a laboratory of the Gertrude E. and John M. Petersen Institute of NanoScience and Engineering, housed at the University of Pittsburgh.

## Conflict of Interest

The authors declare no conflict of interest.

## Data Availability Statement

The data that support the findings of this study are available from the corresponding author upon reasonable request.

## Keywords

dynamic synapses, electrochemical synapses, neuromorphic computing, spatiotemporal dynamics, spiking neural networks, tungsten oxide

Received: February 1, 2021  
Revised: April 12, 2021  
Published online: June 23, 2021

- [1] Q. Wan, M. T. Sharbati, J. R. Erickson, Y. Du, F. Xiong, *Adv. Mater. Technol.* **2019**, *4*, 1900037.
- [2] K. Roy, A. Jaiswal, P. Panda, *Nature* **2019**, *575*, 607.
- [3] Y. LeCun, Y. Bengio, G. Hinton, *Nature* **2015**, *521*, 436.
- [4] A. Krizhevsky, I. Sutskever, G. E. Hinton, *Commun. ACM* **2017**, *60*, 84.
- [5] D. Kuzum, S. Yu, H. S. Philip Wong, *Nanotechnology* **2013**, *24*, 382001.
- [6] N. K. Upadhyay, S. Joshi, J. J. Yang, *Sci. China Inf. Sci.* **2016**, *59*, 061404.
- [7] M. Versace, B. Chandler, *IEEE Spectr.* **2010**, *47*, 30.
- [8] G. Snider, R. Amerson, D. Carter, H. Abdalla, M. S. Qureshi, J. Léveillé, M. Versace, H. Ames, S. Patrick, B. Chandler, A. Gorchetnikov, E. Mingolla, *Computer* **2011**, *44*, 21.
- [9] Y. Ma, Y. Cao, S. Vrudhula, J.-S. Seo, in *Proc. of the 2017 ACM/SIGDA Int. Symp. on Field-Programmable Gate Arrays*, Association for Computing Machinery, Monterey, CA **2017**, p. 45.
- [10] T. K. Horiuchi, T. M. Massoud, presented at *2014 IEEE Biomedical Circuits and Systems Conf. (BioCAS) Proc.*, Lausanne, Switzerland **2014**.
- [11] X. Lagorce, G. Orchard, F. Galluppi, B. E. Shi, R. B. Benosman, *IEEE Trans. Pattern Anal. Mach. Intell.* **2017**, *39*, 1346.
- [12] X. Lagorce, R. Benosman, *Neural Comput.* **2015**, *27*, 2261.
- [13] P. A. Merolla, J. V. Arthur, R. Alvarez-Icaza, A. S. Cassidy, J. Sawada, F. Akopyan, B. L. Jackson, N. Imam, C. Guo, Y. Nakamura, B. Brezoz, I. Vo, S. K. Esser, R. Appuswamy, B. Taba, A. Amir, M. D. Flickner, W. P. Risk, R. Manohar, D. S. Modha, *Science* **2014**, *345*, 668.
- [14] T. Tuma, A. Pantazi, M. Le Gallo, A. Sebastian, E. Eleftheriou, *Nat. Nanotechnol.* **2016**, *11*, 693.
- [15] Z. Wang, S. Joshi, S. Savel'ev, W. Song, R. Midya, Y. Li, M. Rao, P. Yan, S. Asapu, Y. Zhuo, H. Jiang, P. Lin, C. Li, J. H. Yoon, N. K. Upadhyay, J. Zhang, M. Hu, J. P. Strachan, M. Barnell, Q. Wu, H. Wu, R. S. Williams, Q. Xia, J. J. Yang, *Nat. Electron.* **2018**, *1*, 137.
- [16] Z. Wang, B. Crafton, J. Gomez, R. Xu, A. Luo, Z. Krivokapic, L. Martin, S. Datta, A. Raychowdhury, A. I. Khan, presented at *2018 IEEE Int. Electron Devices Meeting (IEDM)*, San Francisco, CA **2018**.
- [17] B. L. Jackson, B. Rajendran, G. S. Corrado, M. Breitwisch, G. W. Burr, R. Cheek, K. Gopalakrishnan, S. Raoux, C. T. Rettner, A. Padilla, A. G. Schrott, R. S. Shenoy, B. N. Kurdi, C. H. Lam, D. S. Modha, *J. Emerg. Technol. Comput. Syst.* **2013**, *9*, 12.
- [18] D. Kuzum, R. G. D. Jeyasingh, B. Lee, H. S. P. Wong, *Nano Lett.* **2012**, *12*, 2179.
- [19] S. Ambrogio, P. Narayanan, H. Tsai, R. M. Shelby, I. Boybat, C. di Nolfo, S. Sidler, M. Giordano, M. Bordini, N. C. P. Farinha, B. Killeen, C. Cheng, Y. Jaoudi, G. W. Burr, *Nature* **2018**, *558*, 60.
- [20] M. Prezioso, F. Merrih-Bayat, B. D. Hoskins, G. C. Adam, K. K. Likharev, D. B. Strukov, *Nature* **2015**, *521*, 61.
- [21] T. Werner, E. Vianello, O. Bichler, D. Garbin, D. Cattaert, B. Yvert, B. De Salvo, L. Perniola, *Front. Neurosci.* **2016**, *10*.
- [22] W. Wang, G. Pedretti, V. Milo, R. Carboni, A. Calderoni, N. Ramaswamy, A. S. Spinelli, D. Ielmini, *Sci Adv.* **2018**, *4*, eaat4752.
- [23] N. Locatelli, V. Cros, J. Grollier, *Nat. Mater.* **2014**, *13*, 11.
- [24] A. F. Vincent, J. Larroque, N. Locatelli, N. B. Romdhane, O. Bichler, C. Gamrat, W. S. Zhao, J. Klein, S. Galdin-Retailleau, D. Querlioz, *IEEE Trans. Biomed. Circuits Syst.* **2015**, *9*, 166.
- [25] S. Oh, T. Kim, M. Kwak, J. Song, J. Woo, S. Jeon, I. K. Yoo, H. Hwang, *IEEE Electron Device Lett.* **2017**, *38*, 732.
- [26] B. Obradovic, T. Rakshit, R. Hatcher, J. Kittl, R. Sengupta, J. G. Hong, M. S. Rodder, *IEEE J. Electron Devices Soc.* **2018**, *6*, 438.
- [27] M. Lee, W. Lee, S. Choi, J.-W. Jo, J. Kim, S. K. Park, Y.-H. Kim, *Adv. Mater.* **2017**, *29*, 1700951.
- [28] Y. Wang, Z. Lv, J. Chen, Z. Wang, Y. Zhou, L. Zhou, X. Chen, S.-T. Han, *Adv. Mater.* **2018**, *30*, 1802883.
- [29] J. Feldmann, N. Youngblood, C. D. Wright, H. Bhaskaran, W. H. P. Pernice, *Nature* **2019**, *569*, 208.
- [30] J. Feldmann, N. Youngblood, M. Karpov, H. Gehring, X. Li, M. Stappers, M. Le Gallo, X. Fu, A. Lukashchuk, A. S. Raja, J. Liu, C. D. Wright, A. Sebastian, T. J. Kippenberg, W. H. P. Pernice, H. Bhaskaran, *Nature* **2021**, *589*, 52.
- [31] a) E. J. Fuller, F. E. Gabaly, F. Léonard, S. Agarwal, S. J. Plimpton, R. B. Jacobs-Gedrim, C. D. James, M. J. Marinella, A. A. Talin, *Adv. Mater.* **2017**, *29*, 1604310; b) X. Yao, K. Klyukin, W. Lu, M. Onen, S. Ryu, D. Kim, N. Emond, I. Waluyo, A. Hunt, J. A. del Alamo, J. Li, B. Yildiz, *Nat. Commun.* **2020**, *11*, 3134; c) Y. Li, J. Lu, D. Shang, Q. Liu, S. Wu, Z. Wu, X. Zhang, J. Yang, Z. Wang, H. Lv, M. Liu, *Adv. Mater.* **2020**, *32*, 2003018; d) Y. Li, E. J. Fuller, J. D. Sugar, S. Yoo, D. S. Ashby, C. H. Bennett, R. D. Horton, M. S. Bartsch, M. J. Marinella, W. D. Lu, A. A. Talin, *Adv. Mater.* **2020**, *32*, 2003984;
- [32] Y. van de Burgt, E. Lubberman, E. J. Fuller, S. T. Keene, G. C. Faria, S. Agarwal, M. J. Marinella, A. Alec Talin, A. Salleo, *Nat. Mater.* **2017**, *16*, 414.
- [33] M. T. Sharbati, Y. Du, J. Torres, N. D. Ardolino, M. Yun, F. Xiong, *Adv. Mater.* **2018**, *30*, 1802353.
- [34] Y. Li, E. J. Fuller, S. Asapu, S. Agarwal, T. Kurita, J. J. Yang, A. A. Talin, *ACS Appl. Mater. Interfaces* **2019**, *11*, 38982.

- [35] E. J. Fuller, S. T. Keene, A. Melianas, Z. Wang, S. Agarwal, Y. Li, Y. Tuchman, C. D. James, M. J. Marinella, J. J. Yang, A. Salleo, A. A. Talin, *Science* **2019**, 364, 570.
- [36] C.-S. Yang, D.-S. Shang, N. Liu, E. J. Fuller, S. Agrawal, A. A. Talin, Y.-Q. Li, B.-G. Shen, Y. Sun, *Adv. Funct. Mater.* **2018**, 28, 1804170.
- [37] J. Zhu, Y. Yang, R. Jia, Z. Liang, W. Zhu, Z. U. Rehman, L. Bao, X. Zhang, Y. Cai, L. Song, R. Huang, *Adv. Mater.* **2018**, 30, 1800195.
- [38] C. Qian, J. Sun, L.-A. Kong, G. Gou, J. Yang, J. He, Y. Gao, Q. Wan, *ACS Appl. Mater. Interfaces* **2016**, 8, 26169.
- [39] Q. Wan, P. Zhang, Q. Shao, M. T. Sharbati, J. R. Erickson, K. L. Wang, F. Xiong, *APL Mater.* **2019**, 7, 101107.
- [40] H. Zheng, J. Z. Ou, M. S. Strano, R. B. Kaner, A. Mitchell, K. Kalantar-zadeh, *Adv. Funct. Mater.* **2011**, 21, 2175.
- [41] J.-T. Yang, C. Ma, C. Ge, Q.-H. Zhang, J.-Y. Du, J.-K. Li, H.-Y. Huang, M. He, C. Wang, S. Meng, L. Gu, H.-B. Lu, G.-Z. Yang, K.-J. Jin, *J. Mater. Chem. C* **2017**, 5, 11694.
- [42] Q. Zhong, J. R. Dahn, K. Colbow, *Phys. Rev. B* **1992**, 46, 2554.
- [43] A. Hjelm, C. G. Granqvist, J. M. Wills, *Phys. Rev. B* **1996**, 54, 2436.
- [44] S.-H. Lee, M. J. Seong, H. M. Cheong, E. Ozkan, E. C. Tracy, S. K. Deb, *Solid State Ion.* **2003**, 156, 447.
- [45] P. M. Wu, S. Ishii, K. Tanabe, K. Munakata, R. H. Hammond, K. Tokiwa, T. H. Geballe, M. R. Beasley, *Appl. Phys. Lett* **2015**, 106, 042602.
- [46] K. Yoshimatsu, T. Soma, A. Ohtomo, *Appl. Phys. Express* **2016**, 9, 075802.
- [47] S. Nishihaya, M. Uchida, Y. Kozuka, Y. Iwasa, M. Kawasaki, S. Nishihaya, M. Uchida, Y. Kozuka, Y. Iwasa, M. Kawasaki, Y. Iwasa, M. Kawasaki, *ACS Appl. Mater. Interfaces* **2016**, 8, 22330.
- [48] X. Leng, J. Pereira, J. Strle, G. Dubuis, A. T. Bollinger, A. Gozar, J. Wu, N. Litombe, C. Panagopoulos, D. Pavuna, I. Božović, *npj Quantum Mater.* **2017**, 2, 35.
- [49] G. Cristiano, M. Giordano, S. Ambrogio, L. P. Romero, C. Cheng, P. Narayanan, H. Tsai, R. M. Shelby, G. W. Burr, *J. Appl. Phys.* **2018**, 124, 151901.
- [50] X. Leng, J. Pereira, J. Strle, A. T. Bollinger, I. Božović, *APL Mater.* **2015**, 3, 096102.
- [51] J.-T. Yang, C. Ge, J.-Y. Du, H.-Y. Huang, M. He, C. Wang, H.-B. Lu, G.-Z. Yang, K.-J. Jin, *Adv. Mater.* **2018**, 30, 1801548.
- [52] J. Tang, D. Bishop, S. Kim, M. Copel, T. Gokmen, T. Todorov, S. Shin, K. Lee, P. Solomon, K. Chan, W. Haensch, J. Rozen, presented at 2018 IEEE Int. Electron Devices Meeting (IEDM), San Francisco, CA **2018**.
- [53] S. Kim, T. Todorov, M. Onen, T. Gokmen, D. Bishop, P. Solomon, K. Lee, M. Copel, D. B. Farmer, J. A. Ott, T. Ando, H. Miyazoe, V. Narayanan, J. Rozen, presented at 2019 IEEE Int. Electron Devices Meeting (IEDM), San Francisco, CA **2019**.
- [54] R.-T. Wen, C. G. Granqvist, G. A. Niklasson, *Nat. Mater.* **2015**, 14, 996.
- [55] F. La Mantia, C. D. Wessells, H. D. Deshazer, Y. Cui, *Electrochem. Commun.* **2013**, 31, 141.
- [56] Y. Li, *Solid State Ion.* **2018**, 323, 142.
- [57] H. Matsui, T. Nakamura, Y. Kobayashi, M. Tabuchi, Y. Yamada, *J. Power Sources* **2010**, 195, 6879.
- [58] G. W. Burr, R. M. Shelby, A. Sebastian, S. Kim, S. Kim, S. Sidler, K. Virwani, M. Ishii, P. Narayanan, A. Fumarola, L. L. Sanches, I. Boybat, M. Le Gallo, K. Moon, J. Woo, H. Hwang, Y. Leblebici, *Adv. Phys.: X* **2017**, 2, 89.
- [59] S. Poongodi, P. S. Kumar, Y. Masuda, D. Mangalaraj, N. Ponpandian, C. Viswanathan, S. Ramakrishna, *RSC Adv.* **2015**, 5, 96416.
- [60] V. I. Shapovalov, A. E. Lapshin, A. G. Gagarin, L. P. Efimenko, *Glass Phys. Chem.* **2014**, 40, 553.
- [61] H. Sakamoto, T. Ariyoshi, N. Kimpara, K. Sugao, I. Taiko, K. Takikawa, D. Asanuma, S. Namiki, K. Hirose, *Nat. Neurosci.* **2018**, 21, 41.
- [62] K. Xu, M. M. Islam, D. Guzman, A. C. Seabaugh, A. Strachan, S. K. Fullerton-Shirey, *ACS Appl. Mater. Interfaces* **2018**, 10, 43166.
- [63] R. S. Zucker, W. G. Regehr, *Annu. Rev. Physiol.* **2002**, 64, 355.
- [64] E. S. Fortune, G. J. Rose, *Trends Neurosci.* **2001**, 24, 381.
- [65] H. Anwar, X. Li, D. Bucher, F. Nadim, *Curr. Opin. Neurol.* **2017**, 43, 71.
- [66] L. Q. Zhu, C. J. Wan, L. Q. Guo, Y. Shi, Q. Wan, *Nat. Commun.* **2014**, 5, 3158.
- [67] H. Akolkar, C. Meyer, X. Clady, O. Marre, C. Bartolozzi, S. Panzeri, R. Benosman, *Neural Comput.* **2015**, 27, 561.
- [68] Y. Mi, X. Lin, S. Wu, *Front. Comput. Neurosci.* **2016**, 10.
- [69] L. Li, Y. Mi, W. Zhang, D.-H. Wang, S. Wu, *Front. Comput. Neurosci.* **2018**, 12.
- [70] D. Buonomano, T. Carvalho, *Front. Integr. Neurosci.* **2011**, 5.
- [71] H. Xu, S. Fathipour, E. W. Kinder, A. C. Seabaugh, S. K. Fullerton-Shirey, *ACS Nano* **2015**, 9, 4900.